18

Reprinted from MONTHLY WEATHER REVIEW, Vol. 117, No. 9, September 1989
American Meteorological Society

# Energetics Examination of Winter Blocking Simulations in the Northern Hemisphere

ERNEST C. KUNG AND H. L. TANAKA*

*Department of Atmospheric Science, University of Missouri—Columbia, Columbia, Missouri*

WAYMAN E. BAKER

*Development Division, National Meteorological Center, NWS/NOAA, Washington, D.C.*

(Manuscript received 16 August 1988, in final form 30 March 1989)

ABSTRACT

Four numerical simulations of the global atmosphere for January 1979 are analyzed to study the formation of blocking in terms of Northern Hemisphere energetics. The Goddard Laboratory for Atmospheres (GLA) 4° × 5° latitude–longitude grid general circulation model (GCM) and 2° × 2.5° grid GCM are employed with the GLA and Geophysical Fluid Dynamics Laboratory (GFDL) initial datasets.

The difficulty in simulating a realistic blocking due to inadequate wave–wave interaction can be attributed in part to inadequate grid resolution. Among four simulations, the simulations by the high resolution GCM produce realistically strong blockings with compatible spectral energetics as in the observed blocking episodes. The latitude–height cross sections of the energy variables of wavenumber 1 is presented to describe the dipole structure of blockings. Blocking development is also examined in time series of barotropic and baroclinic components of energy and associated conversions.

## 1. Introduction

The winter in the Northern Hemisphere is often dominated by a sequence of blocking events, and the ability of general circulation models (GCMs) to simulate blocking is a major concern in producing reasonably accurate short to medium-range forecasts (e.g., Bengtsson 1981; Miyakoda et al. 1983). In Kung and Baker (1986) we compared energetics features associated with observed and simulated blocking situations in the Northern Hemisphere winter. The observed blockings are developed and maintained by the nonlinear transfer of kinetic energy through the wave–wave interaction $L(n)$ from cyclone-scale waves to ultralong waves. The cyclone-scale energy source is provided by baroclinic conversion $C(n)$ from available potential energy to kinetic energy. The simulation, which fails to produce pronounced blocking, converts available potential energy to kinetic energy at all wave ranges. However, the converted energy is either cascaded down to short waves through $L(n)$ or fed to the zonal mean component through wave–mean interaction $M(n)$ without building up the kinetic energy of ultralong waves.

Our finding on the importance of wave–wave interaction in blocking development agrees with Saltzman's (1959) earlier proposal that the large-scale quasi-stationary flow systems are maintained by a nonlinear barotropic transfer of kinetic energy from smaller cyclone-scale disturbances which have baroclinic energy sources. It is also consistent with Hansen and Sutera's (1984) report on the necessity of nonlinear wave–wave interaction in supporting the kinetic energy of blockings, and also with Holopainen and Fortelius' (1987) study which demonstrated that the barotropic energy transfer, from the high-frequency eddies to the time-mean flow, is very strong during the blocking episode. In our recent energetics diagnosis of the observed general circulation in three-dimensional normal mode expansions (Tanaka and Kung 1988), it is shown that an upscale energy cascade during the development of winter blocking in the Northern Hemisphere is accompanied by energy transformation from baroclinic *to* barotropic components. Since blocking is often characterized by its barotropic structure, the barotropic and baroclinic decomposition of normal mode energetics provides additional means for the diagnosis in the zonal wavenumber domain.

It is noted that the separation of energy variables into the standard zonal mean and eddy components does not always permit the simple interpretation of the energetics mechanisms, particularly for a local synoptic system. During the blocking period a distinct local manifestation of the hemispherical circulation is apparent in and around the blocked region. However,

* Present affiliation: Geophysical Institute, University of Alaska—Fairbanks.

*Corresponding author address:* Dr. Ernest C. Kung, Dept. of Atmospheric Science, University of Missouri—Columbia, Columbia, MO 65211.

from the viewpoint of the general circulation, the major blocking such as the Atlantic or Pacific blocking during the winter is not a local system. As shown in Kung and Baker (1986) the development of the Atlantic or Pacific blocking is manifested in $n = 1$, and that of the concurrent two blockings in the Atlantic or Pacific in $n = 2$. During January 1979, the month for which the simulations are analyzed, a typical Pacific blocking was formed in the early part of the month, and a typical Atlantic blocking followed toward the end of the month. Such a large blocking would permit the spectral diagnosis to reveal essential mechanisms of blocking even though it is a case analysis. The hemispherical nature and scale of the major winter blockings will also be demonstrated throughout this paper. The main objective of this paper is to diagnose the blocking simulation in the context of the energetics of the general circulation. A diagnosis of the local energy budget would be desirable; however, this approach will be left for a future study.

Since the simulation failure of winter blocking is attributable to the improper nonlinear wave–wave interaction of kinetic energy in building up the barotropic energy of ultralong waves, it is interesting to see how various simulation conditions affect this part of the energy process. In this study, four numerical simulations of the global atmosphere for January 1979 are analyzed in terms of their Northern Hemisphere energetics. The Goddard Laboratory for Atmospheres (GLA) standard 4° × 5° latitude–longitude grid GCM and high resolution 2° × 2.5° grid GCM are employed for blocking simulation, each with the GLA and Geophysical Fluid Dynamics Laboratory (GFDL) initial datasets for 0000 UTC 1 January 1979. The development of blocking is identified, and its extent and pattern examined, for each simulation. Through intercomparison among simulations and comparison with observations by Kung and Baker (1986) and Tanaka and Kung (1988), an energetics assessment is performed for these simulations. The standard spectral energetics in the zonal wavenumber domain and three-dimensional normal mode energetics are both used in this study to supplement each other.

## 2. Simulation experiments and datasets

Four simulation experiments (Expts. 1, 2, 3 and 4) were conducted for the period of 1–31 January 1979 with the GLA standard and high resolution GCMs (see Table 1). The GLA and GFDL gridded analyses of the First GARP (Global Atmospheric Research Program) Global Experiment (FGGE) at 0000 UTC 1 January were used as the initial data (see Daley et al. 1985; Kung and Baker 1986). The mean January climatology of the sea surface temperature was used in all four simulations.

The standard coarse resolution GLA GCM used in simulation experiments is the fourth-order global atmospheric model described by Kalnay-Rivas et al. (1977) and by Kalnay et al. (1983). There are nine vertical layers equal in sigma with a uniform nonstaggered horizontal grid of 4° latitude by 5° longitude. It is based on an energy conserving scheme in which all horizontal differences are computed with fourth-order accuracy. A 16th-order Shapiro (1970) filter is applied every 2 hours on the sea level pressure, potential temperature, and wind fields. In this scheme, wavelengths longer than four grid lengths are resolved accurately without damping. Wavelengths shorter than four grid lengths, which would otherwise be grossly misrepresented by the finite differences, are filtered out while they are still infinitesimal. The 2° latitude by 2.5° longitude version (high resolution version) of the GLA GCM is identical to the coarse resolution version with respect to the physical parameterizations. The timestep of the hydrodynamics is 3.75 min in the high resolution version compared to 7.5 min in the coarse resolution version and an eighth-order Shapiro (1970) filter is used rather than the 16th-order filter used in the coarse resolution model.

TABLE 1. Four simulation experiments of the January 1979 global atmosphere with GLA GCMs, and blocking episodes identified in the observed and simulated Northern Hemisphere circulation. The observed periods are after Kung and Baker (1986).

| | GCM grid (latitude × longitude) | 1/1/79 0000 UTC initial data | Blocking period (day/mo/yr) |
|---|---|---|---|
| Observation | — | — | 5/1–14/1/79 |
| | | | 15/1–29/1/79 |
| Expt. 1 | 4° × 5° | GLA | 10/1–14/1/79 |
| Expt. 2 | 4° × 5° | GFDL | 9/1–13/1/79 |
| Expt. 3 | 2° × 2.5° | GLA | 4/1–13/1/79 |
| | | | 22/1–26/1/79 |
| | | | 29/1–31/1/79 |
| Expt. 4 | 2° × 2.5° | GFDL | 8/1–11/1/79 |

The GLA analysis scheme (Baker 1983) used to produce initial conditions for Expts. 1 and 3, as summarized in Daley et al. (1985), employs a univariate successive correlation method for the height, horizontal wind components, and relative humidity on pressure surfaces. All of the analyses are smoothed and then analysis-minus-first-guess differences are interpolated to the model sigma levels. The assimilation procedure involves the intermittent analysis of batches of data grouped in a ±3 h window about each synoptic time. The wind and height fields are updated independently without any explicit coupling or balancing. In contrast to the GLA approach, the GFDL assimilation procedure employs a spectral, rhomboidal 30, 18 level, general circulation model with continuous data insertion at every time step. The objective analysis scheme used to provide the initial conditions for Expts. 2 and 4, (see Daley et al. 1985), utilizes a univariate optimum interpolation procedure on pressure surfaces. Nonlin-

ear normal mode initialization is applied every 6 hours during the assimilation.

The four simulation datasets and GLA gridded data of the FGGE observations analyzed in this study include twice-daily values of geopotential height, temperature, humidity, horizontal wind and vertical velocity at 0000 and 1200 UTC, which are given on the $4° \times 5°$ latitude–longitude grid at 1000, 850, 700, 500, 400, 300, 250, 200, 150, 100, 70, and 50 mb at 0000 and 1200 UTC.

## 3. Scheme of analysis

Table 2 lists symbols, definitions, and variables used in this paper. The computational analysis of the standard spectral energetics in the zonal wavenumber domain is based on Saltzman's (1957, 1970) formulation of equations of kinetic energy:

$$\frac{\partial K(0)}{\partial t} = \sum_{n=1}^{N} M(n) + C(0) - D(0) \qquad (1)$$

$$\frac{\partial K(n)}{\partial t} = -M(n) + L(n) + C(n) - D(n), \quad n \neq 0. \qquad (2)$$

Equations (1) and (2) state the balance requirement over the total mass of the atmosphere in a closed domain. In this study, transformation terms are obtained so that the energy equations also hold at each point in the meridional–height cross section. This is done by the use of the advective form instead of the convergence form in computing the nonlinear interaction terms $M(n)$ and $L(n)$, and also by replacing $C(n)$ with $-\mathbf{V}\cdot\nabla\Phi$ at $n$. For the discussion of baroclinic conversion, $C(n)$ is computed explicitly with the vertical motion and specific volume. In computing spectral energetics over the Northern Hemisphere, the energetics variables evaluated in the meridional–height cross section are integrated over the Northern Hemisphere. The dissipation terms $D(n)$ of kinetic energy in Eqs. (1) and (2) are obtained as residual terms to balance the respective equations. The maximum wavenumber computed for energy variables is $n = 36$.

The analysis scheme of normal mode energetics is based on Tanaka (1985) and Tanaka and Kung (1988). The equation of total energy, $E = K + P$ for a component of three-dimensional normal mode expansion may be written as

$$\partial E_{nlm}/\partial t = A_{nlm} + B_{nlm} + F_{nlm}. \qquad (3)$$

The total energy pertaining to $m = 0$ is defined as barotropic energy, whereas the sum of the energy for $m \neq 0$ is baroclinic energy. The maximum vertical index computed is $m = 10$. The construction of basis functions for very small equivalent height beyond $m = 10$ is very difficult and quite unpredictable. A total of 50 meridional indices are used in this study, including 26 Rossby modes, 12 eastward gravity modes, and 12 westward gravity modes, which are sufficient to describe the large-scale energy characteristics (see Tanaka 1985). The zonal wavenumber $n$ is truncated at $n = 15$. Surface wind at $p = p_s$ has been assumed to vanish as in Tanaka and Kung (1988).

TABLE 2. Symbols, definitions, and variables.

| | |
|---|---|
| $t$ | time |
| $p$ | pressure |
| $p_s$ | constant surface pressure |
| $\mathbf{V}$ | horizontal wind vector |
| $u$ | zonal wind speed |
| $v$ | meridional wind speed |
| $\Phi$ | geopotential |
| $n$ | zonal wavenumber |
| $l$ | meridional index |
| $m$ | vertical index |
| $h_m$ | equivalent height for $m$th vertical index |
| $w_{nlm}$ | three-dimensional spectral expansion coefficient |
| $\nabla$ | horizontal del operator along an isobaric surface |
| $\sigma$ | sigma $(p/p_s)$ |
| $g$ | acceleration of gravity |
| $\rho_0$ | basic density |
| $H$ | scale height of the isothermal atmosphere |
| $\lambda$ | longitude |
| $I$ | blocking index as defined in Eq. (4) |
| $Z$ | geopotential height of the 500 mb surface |
| $z(n)$ | geopotential height at wavenumber $n$ normalized by the factor $\sigma^{1/2}$ |
| $K(n)$ | kinetic energy at wavenumber $n$ |
| $M(n)$ | transfer of $K(n)$ to $K(0)$ where $n \neq 0$ |
| $L(n)$ | transfer of eddy kinetic energy from all other wavenumbers to $K(n)$ where $n \neq 0$ |
| $C(n)$ | conversion of $P(n)$ to $K(n)$ |
| $D(n)$ | dissipation of $K(n)$ |
| $-\mathbf{V}\cdot\nabla\Phi$ | production of kinetic energy by cross-isobaric motion |
| $K$ | kinetic energy over the total mass of the atmosphere |
| $P$ | available potential energy over the total mass of the atmosphere |
| $E$ | total energy, $K + P$ |
| $B$ | nonlinear interaction of $K$ |
| $A$ | nonlinear interaction of $P$ |
| $F$ | net energy source and sink due to diabatic processes over the total mass of the atmosphere |
| ERR | error variance for simulations |

Using the method of normal mode expansion, we can assess the forecast error in the simulated atmosphere by the distance between the spectral expansion coefficients of observation $w_{nlm}$ and simulation $\hat{w}_{nlm}$, where the caret designates variables for simulations. The error variance ERR in simulations may be given as a sum of the following quantities of the normal mode expansion:

$$\mathrm{ERR}_{nlm} = \frac{1}{2} p_s h_m |\hat{w}_{nlm} - w_{nlm}|^2. \qquad (4)$$

A dimensional factor $p_{shm}$ is used so that the error variance has physical units of J m$^{-2}$. By means of the inverse transforms of vertical and Fourier–Hough transforms, it may be shown that the sum of $\mathrm{ERR}_{nlm}$

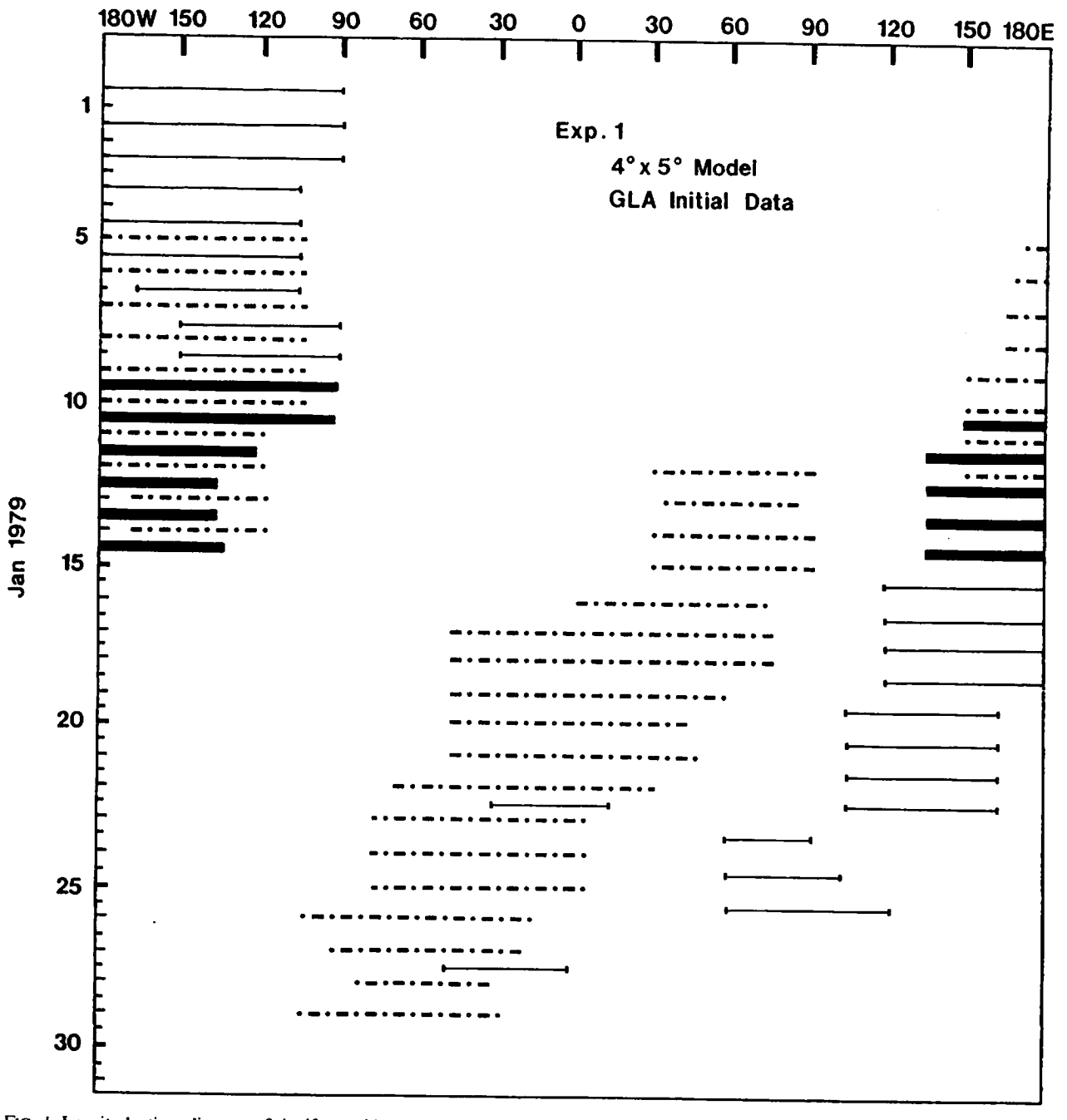


FIG. 1. Longitude–time diagram of significant ridges as noted by horizontal bars during January 1979 in Expt. 1 as identified in the daily 0000 UTC 500 mb charts. Bold lines are for blocking. Dot–dashed lines are for observed blockings after Kung and Baker (1986).

has the same form as total energy $E = K + P$, in which the dependent variables $u$, $v$, and $\Phi$ have been replaced by $\hat{u} - u$, $\hat{v} - v$, and $\hat{\Phi} - \Phi$.

For energetics analysis over the Northern Hemisphere, the basic variables are expanded in the vertical normal modes and zonal harmonics without further expansion in Hough functions. The energetics variables of barotropic and baroclinic components are then integrated over the hemisphere. In this case spectral components of cross-equatorial flux are involved in the energy balance. However, it has been confirmed (Kung 1988) that contributions from such cross-equatorial flux are negligibly small in the observed atmosphere except for $n = 0$. This situation is also the same for all simulations in this study. Unless stated otherwise, the results of $E_{nlm}$, $A_{nlm}$ and $B_{nlm}$ in this study are computed based on the Northern Hemisphere data.

Standard spectral energetics for the observed blocking situation as compared with simulations in this study are adopted from Kung and Baker (1986), and the normal model energetics from Tanaka and Kung (1988). Additional energetics computations for the

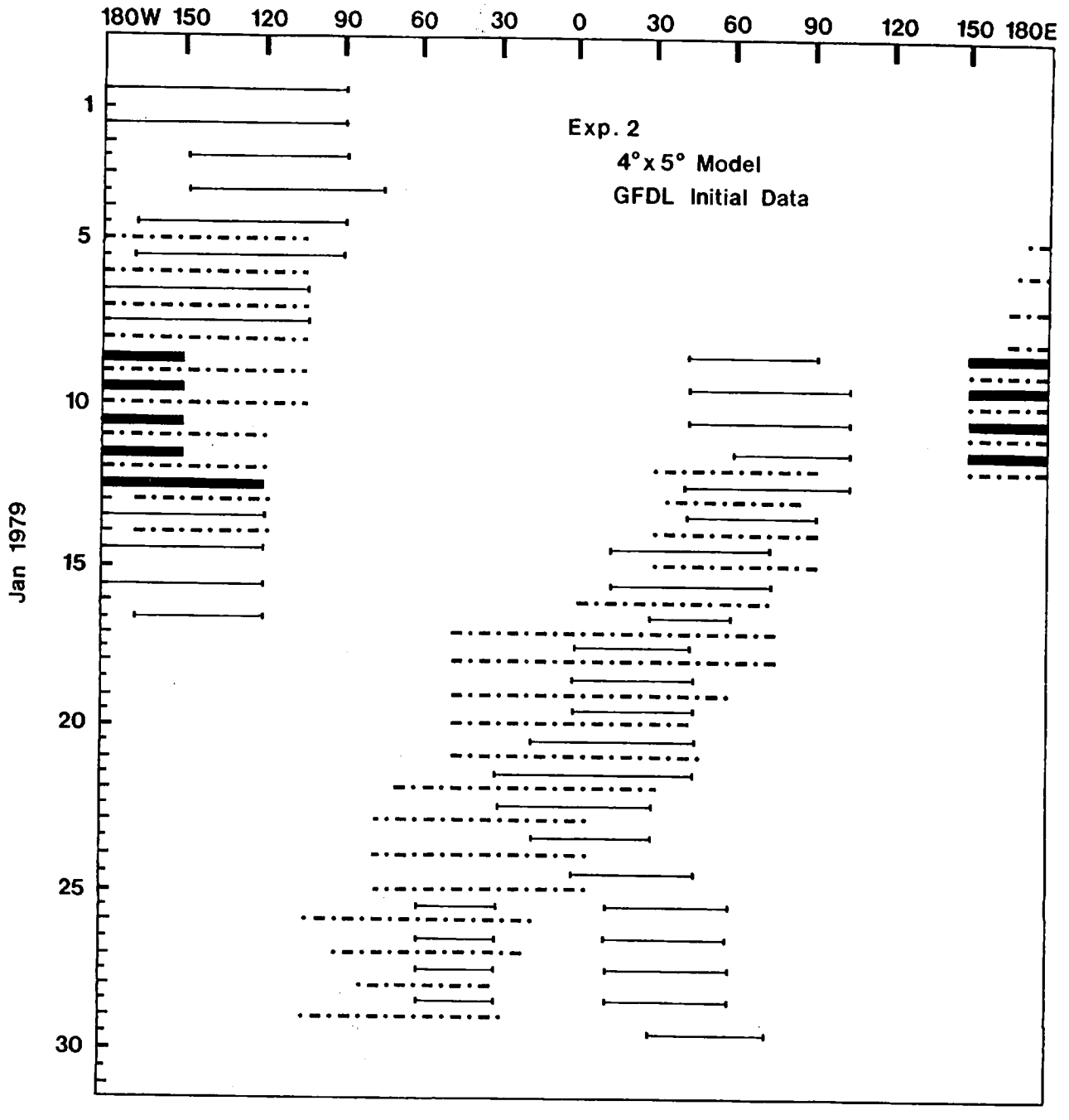


FIG. 2. As in Fig. 1, but for Expt. 2.

observed circulation as needed is performed with the GLA gridded analysis of the FGGE observations.

## 4. Simulated blockings and spectral energetics

Following the procedures of Kung and Baker (1986), the longitudinal width of significant ridges in the 46°–66°N belt are identified with the daily 500 mb charts of the simulated circulation in Figs. 1–4 for the four simulations. The horizontal segments in the longitude–time diagrams represent the longitudinal sector, in which the westerly flow is interrupted because of the presence of ridges. The blocking cases are further identified as bold lines for these longitudinal sectors. A blocking is recognized when the following index $I$ at longitude $\lambda$ is greater than 50 m along the longitudinal sector in the figures:

$$I(\lambda) = Z(\lambda, 66°\text{N}) - Z(\lambda, 46°\text{N}) \qquad (5)$$

where $Z$ is the geopotential height at 500 mb. This criterion is based on the common characteristic of diffluent and meridional types of blocking. In both types of blocking, a quasi-meridional dipole is formed by a

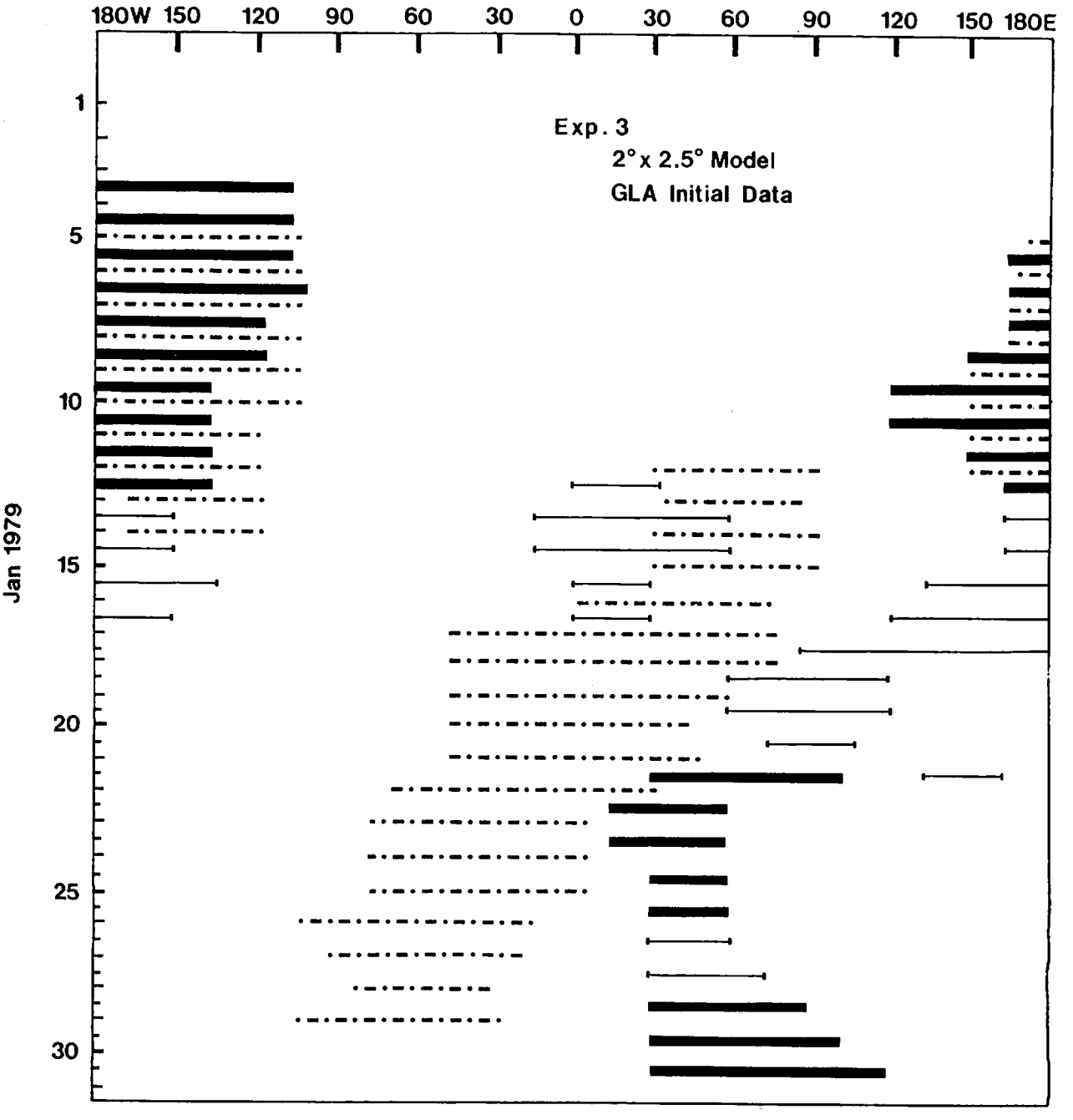


FIG. 3. As in Fig. 1, but for Expt. 3.

high pressure cell poleward and a low pressure area equatorward (see Lejenäs and Økland 1983). For the cases of tilted orientation of meridional dipole, and cases of blocking which are partially out of the chosen latitudinal band, $Z(\lambda \pm 5°, 66°N)$ is substituted for $Z(\lambda, 66°N)$ in Eq. (5) in the additional scan of the circulation pattern. The blocking identification in this method is verified to be consistent with the results of careful manual inspection of the flow pattern (see Kung and Baker 1986). Figures 1–4 also contrast the simulated blockings with the observed blockings by Kung and Baker which are shown with dot–dashed lines.

The periods of identified blocking episodes in the Northern Hemisphere are listed for the four simulations and compared with those of the observed episodes in Table 1. Comparing the simulated blockings with those observed for their latitudinal locations (Figs. 1–4) and periods (Figs. 1–4 and Table 1), it is apparent that there is a considerable difference between the simulation and observation and among the four simulations. The simulations in Expts. 1 and 2 have much shorter blocking periods than the observation. The longitudinal extents of the simulated blockings are more limited than the observation, and some dislocation of blocks

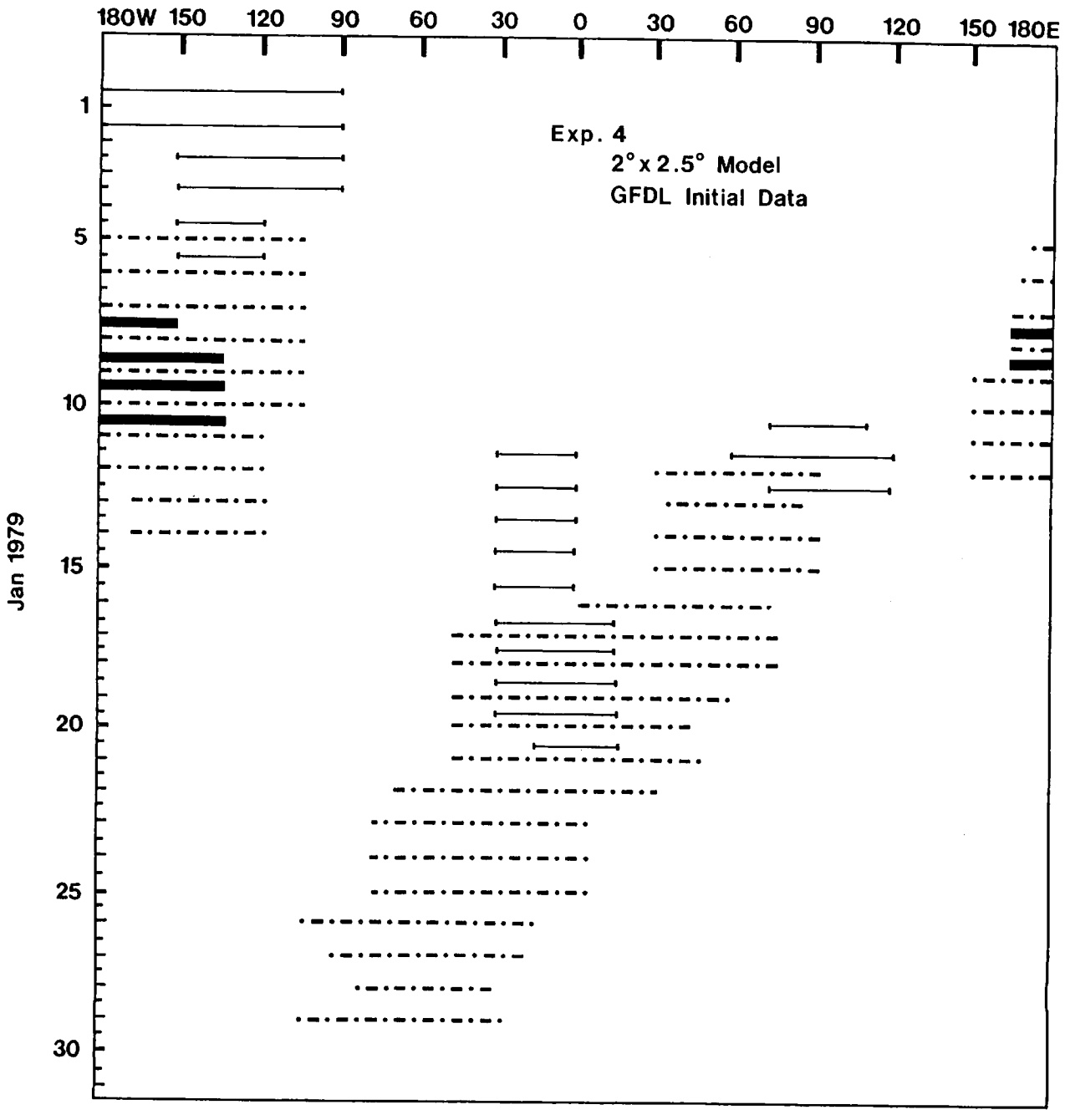


FIG. 4. As in Fig. 1, but for Expt. 4.

is apparent. Figures 5 and 6 verify that the Pacific blocking episodes in Expts. 1 and 2 are much weaker than those of the observation and Expts. 3 and 4. The circulation patterns in Figs. 5 and 6 are for a 5-day period synchronized at 9–13 January. Among the simulations, Expts. 3 and 4 by the high resolution GCM were able to generate realistically strong blocking. Expt. 3 is noted for its large amplitude of blocking, and Expt. 4 for its close resemblance of the phase of the block to that of the observation. Figure 3 also indicates that Expt. 3 produced another blocking episode toward the end of the simulation period although the block is dislocated to the east of the observed block. This is a distinct contrast to the other three simulations in that it was able to amplify the ultralong waves through the entire 1-month period of simulation.

Figure 7 illustrates the error variance growth of the simulations for zonal eddies ($n$ = 1–15) starting from the initial data of 0000 UTC 1 January. The GFDL analyses of the FGGE are used to represent the observed atmosphere for evaluating the prediction error in model simulations. For comparison, the persistence error is presented starting from the same date. The persistence error reaches its saturation level around

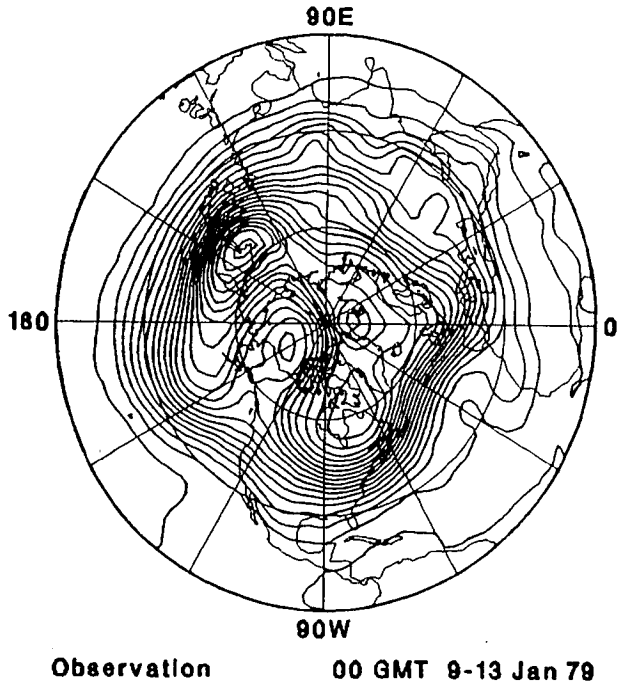


FIG. 5. Observed 5-day mean 500 mb circulation during the Pacific blocking.

days 4 to 6. In contrast, the simulation error energies reach their saturation levels around 8 to 10. Evidently, the high resolution models (solid line) perform better compared to the low resolution models (dotted line). According to Dalcher and Kalnay (1987), the dynamical predictability of a model is determined by the day when the error energy reaches 95 percent of the saturated level. Growing prediction errors show the predictability limits of GLA model simulations at about 7 to 10 days for Expts. 1 to 4.

The circulation patterns of simulations, as shown in Fig. 6, indicate certain predictability of GCMs in blocking formation during the period of 9–13 January. In particular, Expts. 3 and 4 by the high resolution GCM formed a clear, major blocking in the Pacific which is comparable with the observation. This seeming inconsistency with the forecast skill, as shown in Fig. 7, may be explained by a scale dependency of predictability in the atmospheric circulation. Bengtsson (1981) found that the atmospheric predictability increases in a blocking situation. Shukla's (1981) study indicated that ultralong waves possess considerable extended predictability (up to 30–45 days) when compared to shorter waves. This is confirmed collectively by contributors in Holloway and West (1984). Since the prediction error variance in Fig. 7 is for the summation of zonal eddies $n$ = 1–15, it indicates the predictability of the total field of motion rather than that of ultralong waves which are responsible for blocking formation. From Fig. 7 it is apparent that Expt. 4 was the best of the four simulations of the Northern Hemisphere circulation after the error energy reached a saturation level. Presumably, however, due to extended predictability of ultralong waves, Expt. 3 was also able to form a distinct blocking pattern over the Pacific.

The baroclinic conversion $C(n)$, wave–wave interaction $L(n)$, wave–mean interaction $M(n)$, and dissipation $D(n)$ over the Northern Hemisphere for the observed circulation and four simulations are listed in Table 3 for $n$ = 1–36 for the period 5–9 January 1979 when the blocking is in the developmental stage. These four transformation variables determine the eddy kinetic energy blance of individual wavenumbers. Kung and Baker (1986) showed that the change in the available potential energy occurs following the blocking development rather than preceding the blocking. This is consistent with the basically barotropic nature of blocking development, and the budget of available potential energy needs not be examined in this study in connection with blocking development.

It is apparent that the resemblance between energetics is stronger for the two high resolution simulations than for the two low resolution cases. Both Expts. 3 and 4 show large $L(1)$ as in the observed blocking. In contrast, Expts. 1 and 2 have significantly weak $L(1)$ and large energy input at the shortwave range $L(11$–$36)$. It is also apparent that in the high resolution simulations, Expts. 3 and 4, an upscale input to $n$ = 1 is provided through the wave–wave interaction $L(1)$ from the source at the synoptic-scale range, including the contribution from $L(3)$ and $L(4)$. Although $L(1)$ in Expts. 3 and 4 is large, it is still smaller than that in the observation, whereas $L(2)$ is noticeably larger. In comparing Expts. 3 and 4, Expt. 3, with the GLA initial data, seems to provide better energy input at $n$ = 1. As in the observation, Expts. 3 and 4 show positive values of $L(5)$, but they are smaller than that in the observation. In the computation of $L(n)$ no adjustment is made to ensure the balance among wavenumbers. It is seen that the values of $L(1$–$36)$ in the observation and Expt. 3 are reasonably small, whereas those in Expts. 1 and 2 are very large. The large residual values of $L(1$–$36)$ are attributable to the fact that the integration is only for the Northern Hemisphere, and also to the application of Shapiro (1970) filtering in the model integration, which will result in an inconsistency of simulation data with diagnostic equations. These effects are apparently minimized in Expt. 3.

The wave–mean interaction $M(n)$ as shown in Table 3 seems to indicate that its spectral distribution is affected by the initial data. For Expts. 1 and 3 with the GLA initial data a comparable wave–mean interaction with the observation at the synoptic and shortwave range $n$ = 5–36 is indicated. When the GFDL data are used to initialize the high resolution GLA GCM in Expt. 4, a very large flow of kinetic energy from eddies to the zonal mean motion is observed at $n$ = 3 and 6–10, an obvious distortion of energy flow in view of the observed values. This may have prevented a stronger

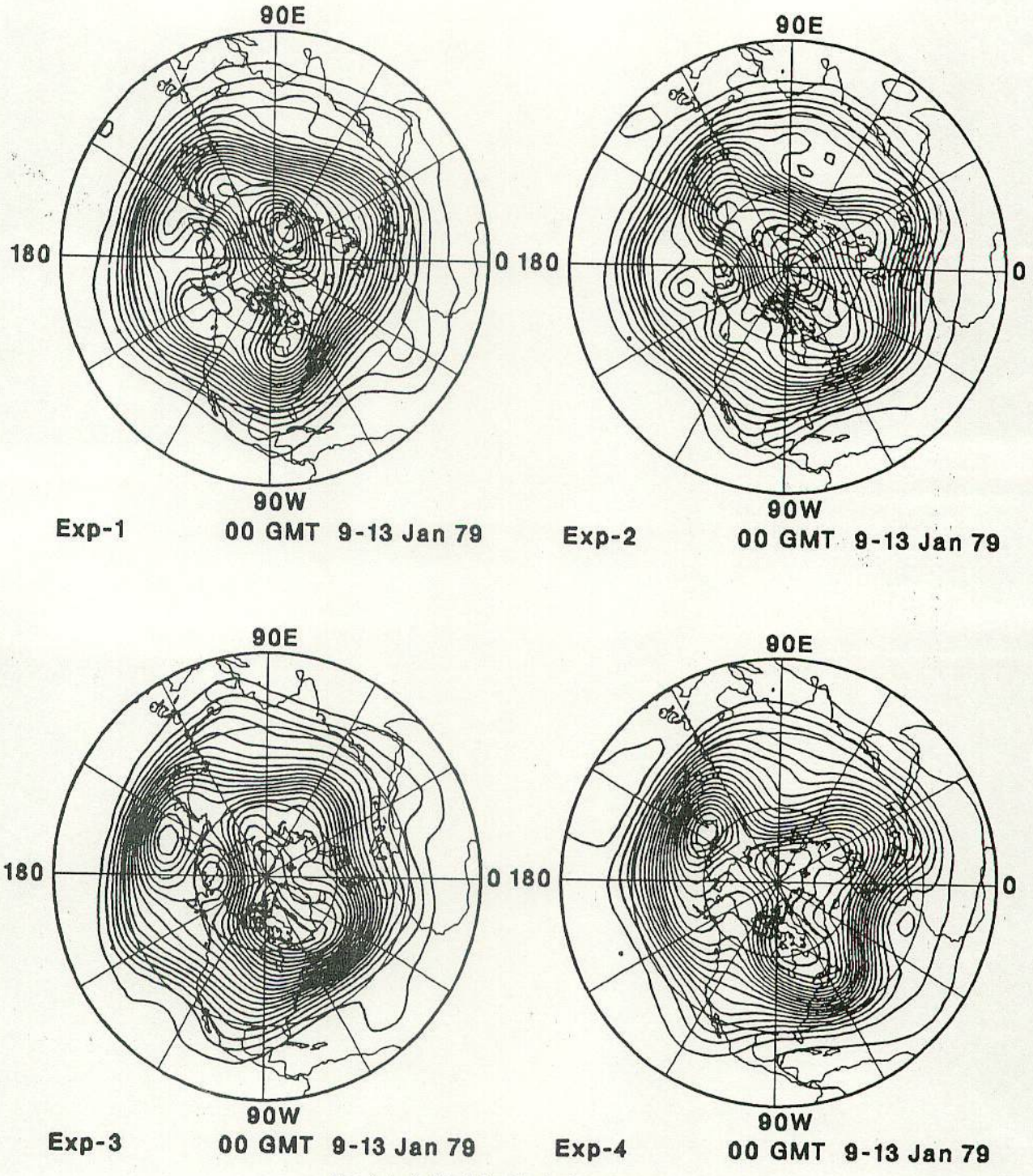


FIG. 6. As in Fig. 5, but for the four simulations.

input in Expt. 4 at $n = 1$ as shown in a relatively weak $L(1)$ in comparison with that in Expt. 3. It appears that the model influence contained in the initial data may amplify in a GCM integration, particularly when the high resolution GCM is used in simulation.

There is a sufficient baroclinic conversion $C(n)$ in all simulations to provide the energy source for barotropic processes of $L(n)$ and $M(n)$. The simulations actually generate more kinetic energy than the observations, which is enhanced in the high resolution simulation. The $C(1\text{–}36)$ in Expts. 3 and 4 is more than 30% higher than in the observation. There are some notable differences in $C(n)$ at the ultralong-wave range among simulations. However, the patterns in this are not identified with any specified differences among experiments. All simulations have more than enough

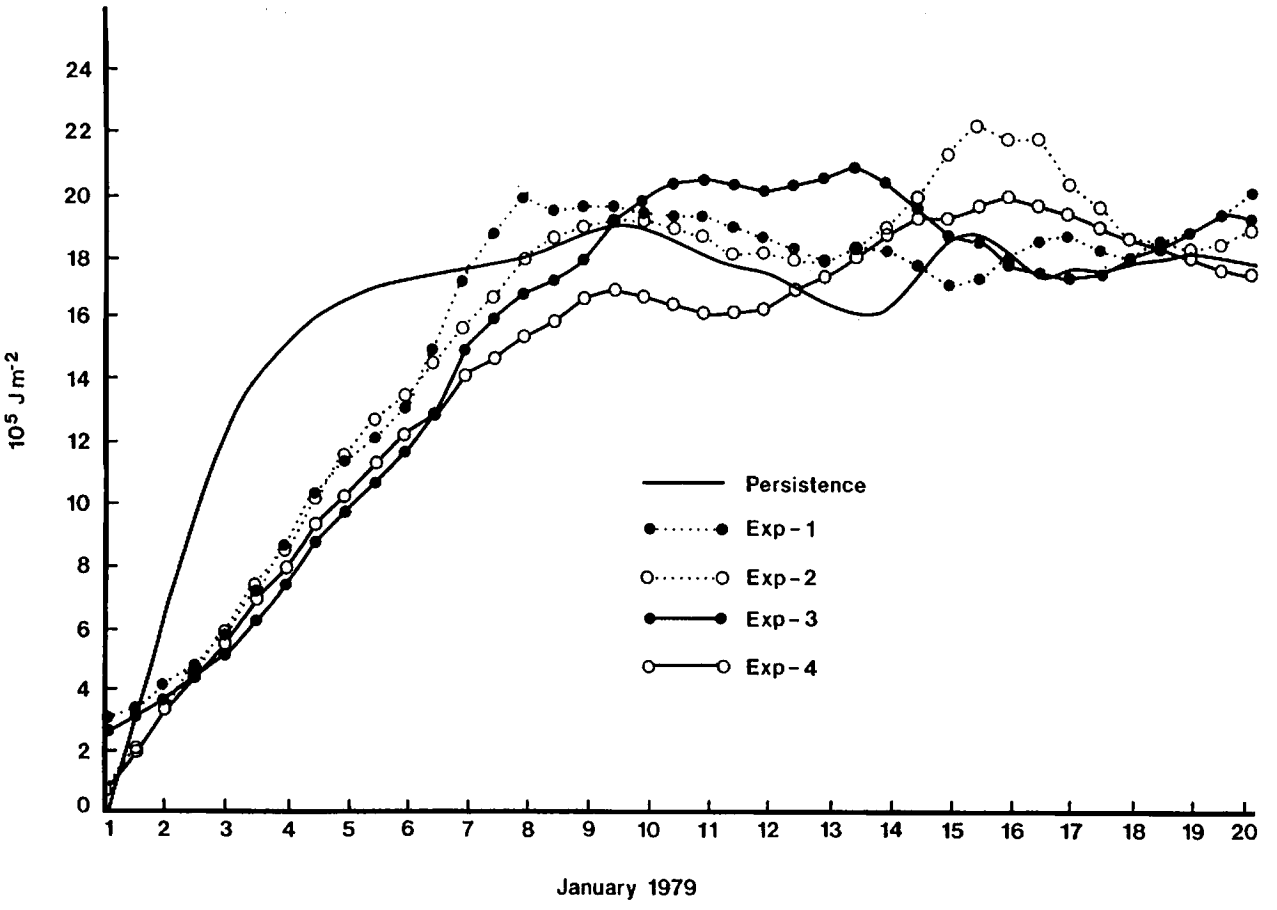


FIG. 7. Growth of prediction error variance for $n$ = 1–15 in Expts. 1 to 4. Persistence error starting from 1 January is indicated by solid line without a dot.

baroclinic energy sources, but the barotropic part of transformations tend to fail to provide as much kinetic energy input at $n$ = 1 as in the observation.

The value $D(n)$ obtained as the residual term of Eq. (2), which is customarily referred to as dissipation, represents the sink of kinetic energy from the specified scale $n$. Thus $D(n)$ can be any process of energy cascade by the scales of motion that cannot be observed with the given grid resolution. All four simulations differ from the observation in their respective spectral distribution of $D(n)$. While the observation shows its maximum dissipation at $n$ = 2 and 3, the simulations have their large dissipation in the shorter wave range $n$ = 6–36. It is particularly noteworthy that the simulations with the coarse grid GCM, Expts. 1 and 2, have a very high dissipation at the shortwave range of $n$ = 11–36. This is consistent with the fact that these simulations generate unduly intense circulation at shortwave range (see Baker and Brin 1985), which shows a marked improvement with the high resolution GCM.

From the listing of eddy kinetic energy transformations, it is apparent that the failure in simulating the realistic blocking can be attributed in part to inadequate grid resolution. The coarse 4° × 5° grid of the standard GLA GCM results in the downscale energy cascade, preventing a proper upscale input at $n$ = 1. It is also shown that the differences in initial datasets obviously result in differences in the spectral energetics. The high resolution GLA GCM with the GFDL initial data produced excessively strong wave-mean interaction, which may have prevented the wave-wave interaction $L(1)$ from reaching a level close to that of the observation. It is relevant to point out that the spectral energetics obtained in this study are for the entire Northern Hemisphere. Our ongoing study indicates that the energetics budget acquired for a limited latitudinal belt of blocking formation, is comparable to that of the Northern Hemisphere, and the energetics characteristics, as discussed above, will be seen more clearly.

## 5. Dipole structure

The widely recognized common characteristic of the blocking situation is the quasi-meridional dipole structure, as shown in Fig. 5 in connection with the fully developed Pacific blocking. In the zonal spectral analy-

TABLE 3. Transfer of eddy kinetic energy by eddy conversion $C(n)$, wave–wave interaction $L(n)$, wave–mean interaction $M(n)$, and dissipation $D(n)$ over the Northern Hemisphere in the observed and simulated circulation for the period 5–9 January 1979. The observed values are taken from Kung and Baker (1986). Units are $10^{-2}$ W m$^{-2}$.

| Datasets | $C(1)$ | $C(2)$ | $C(3)$ | $C(4)$ | $C(5)$ | $C(6–10)$ | $C(11–36)$ | $C(1–36)$ |
|---|---|---|---|---|---|---|---|---|
| Observation | 2 | 50 | 64 | 30 | 41 | 99 | 30 | 316 |
| Expt. 1 | −5 | 20 | 20 | 44 | 80 | 153 | 73 | 385 |
| Expt. 2 | 27 | 8 | 56 | 37 | 34 | 155 | 74 | 391 |
| Expt. 3 | 18 | 29 | 30 | 59 | 64 | 151 | 70 | 421 |
| Expt. 4 | 6 | 50 | 75 | 50 | 45 | 149 | 57 | 432 |
| Datasets | $L(1)$ | $L(2)$ | $L(3)$ | $L(4)$ | $L(5)$ | $L(6–10)$ | $L(11–36)$ | $L(1–36)$ |
| Observation | 67 | 2 | −25 | −22 | 26 | −56 | 7 | −1 |
| Expt. 1 | 24 | −1 | −30 | −13 | −16 | −50 | 17 | −69 |
| Expt. 2 | 16 | 29 | −48 | −18 | −11 | −68 | 23 | −77 |
| Expt. 3 | 52 | 10 | −33 | −18 | 10 | −25 | 9 | 5 |
| Expt. 4 | 42 | 6 | −22 | −22 | 8 | −11 | 16 | 17 |
| Datasets | $M(1)$ | $M(2)$ | $M(3)$ | $M(4)$ | $M(5)$ | $M(6–10)$ | $M(11–36)$ | $M(1–36)$ |
| Observation | 19 | −5 | 2 | 0 | 16 | 15 | −2 | 45 |
| Expt. 1 | −3 | −4 | 8 | 4 | 25 | 15 | −3 | 42 |
| Expt. 2 | 8 | −6 | 9 | 2 | 5 | 8 | −2 | 24 |
| Expt. 3 | 8 | −6 | 1 | 12 | 21 | 19 | 1 | 56 |
| Expt. 4 | 10 | −4 | 40 | 13 | 2 | 41 | 3 | 105 |
| Datasets | $D(1)$ | $D(2)$ | $D(3)$ | $D(4)$ | $D(5)$ | $D(6–10)$ | $D(11–36)$ | $D(1–36)$ |
| Observation | 31 | 73 | 69 | 26 | 28 | 44 | 38 | 309 |
| Expt. 1 | 22 | 17 | 25 | 21 | 20 | 69 | 140 | 314 |
| Expt. 2 | 20 | 22 | 31 | 24 | 15 | 84 | 132 | 328 |
| Expt. 3 | 34 | 35 | 30 | 31 | 40 | 86 | 89 | 345 |
| Expt. 4 | 28 | 41 | 28 | 18 | 30 | 76 | 76 | 297 |

sis of the isobaric height field of the observed circulation, this dipole structure is apparent as the amplitude maxima for $n = 1$ at 45° and 75°N, as shown in the latitude–height cross section of Fig. 8, but not for other wavenumbers. The cross section is for the period 7–11 January when the Pacific blocking is in its full development. The hemispherical scale of this blocking episode is confirmed by the fact that its structure is adequately described by $n = 1$, as shown in Fig. 8. To remove the effects of the density stratification at high altitudes, which results in the large amplitudes of the geopotential and wind fields, the vertical structure of geopotential height is multiplied by $\sigma^{1/2}$ where $\sigma = p/p_s$, and those of energy and energy transformations with the basic density of $\rho_0 = p(gH)^{-1}$ where $H = 8000$ m (see Matsuno 1970) in the latitude–height cross sections shown in this paper. The vertical coordinate in Figs. 8–13 is calibrated by $H \times \ln(p_s/p)$ in the unit of $m$.

The latitude–height distribution of kinetic energy for $n = 1$, as shown in Fig. 9, is consistent with that of $Z(1)$ in Fig. 8. The two cores of maximum kinetic energy between 50° and 60°N and around 80°N are the projection of a fully developed blocking situation. The partition of $K(1)$ into the $u$ and $v$ components in the same figure further indicates that, for the 50°–60°N core the zonal component is the sole contributor, whereas the core at the higher latitudes is supported by both meridional and zonal components. The sources of kinetic energy are examined in Fig. 10. The latitudinal distribution of kinetic energy production $-\mathbf{V}\cdot\nabla\Phi$ for $n = 1$ is consistent with that of $K(1)$. At these latitudes of maximum $K(1)$, the kinetic energy is produced in the lower and upper troposphere to support the circulation against the dissipation. In terms of nonlinear wave–wave interaction $L(1)$, the kinetic energy input at $n = 1$ from the shorter waves has two clearly identified maxima where the two cores of maximum kinetic energy are observed. The wave–mean interaction $M(1)$ shows that its latitude–height distribution does not appear to be related to the dipole structure of blocking.

As shown in Kung and Baker (1986), in the observed circulation the baroclinic energy conversion $C(1)$ is not directly related to the blocking development. The baroclinic energy source always exists in a sufficient amount to support the circulation against the dissipation and to provide the kinetic energy source for nonlinear interactions. This is seen in the consistency of $K(1)$ and $-\mathbf{V}\cdot\nabla\Phi$ for $n = 1$ in their latitudinal variations. The appearance of $L(1)$ maxima at the core regions of kinetic energy maximum is a specific phenomenon in association with the development of blocking, and disappears once the blocking enters the decaying stage.

In comparing the latitude–height cross sections of simulations with those of the observed circulation, the differences in the dipole structure of blocking are striking. Except for Expt. 3, all other simulations show weak dipoles in terms of $K(1)$ in Fig. 11 in comparison with the observation in Fig. 9. It is stronger in Expt. 3 but is still weaker than that in the observation. For Expt.

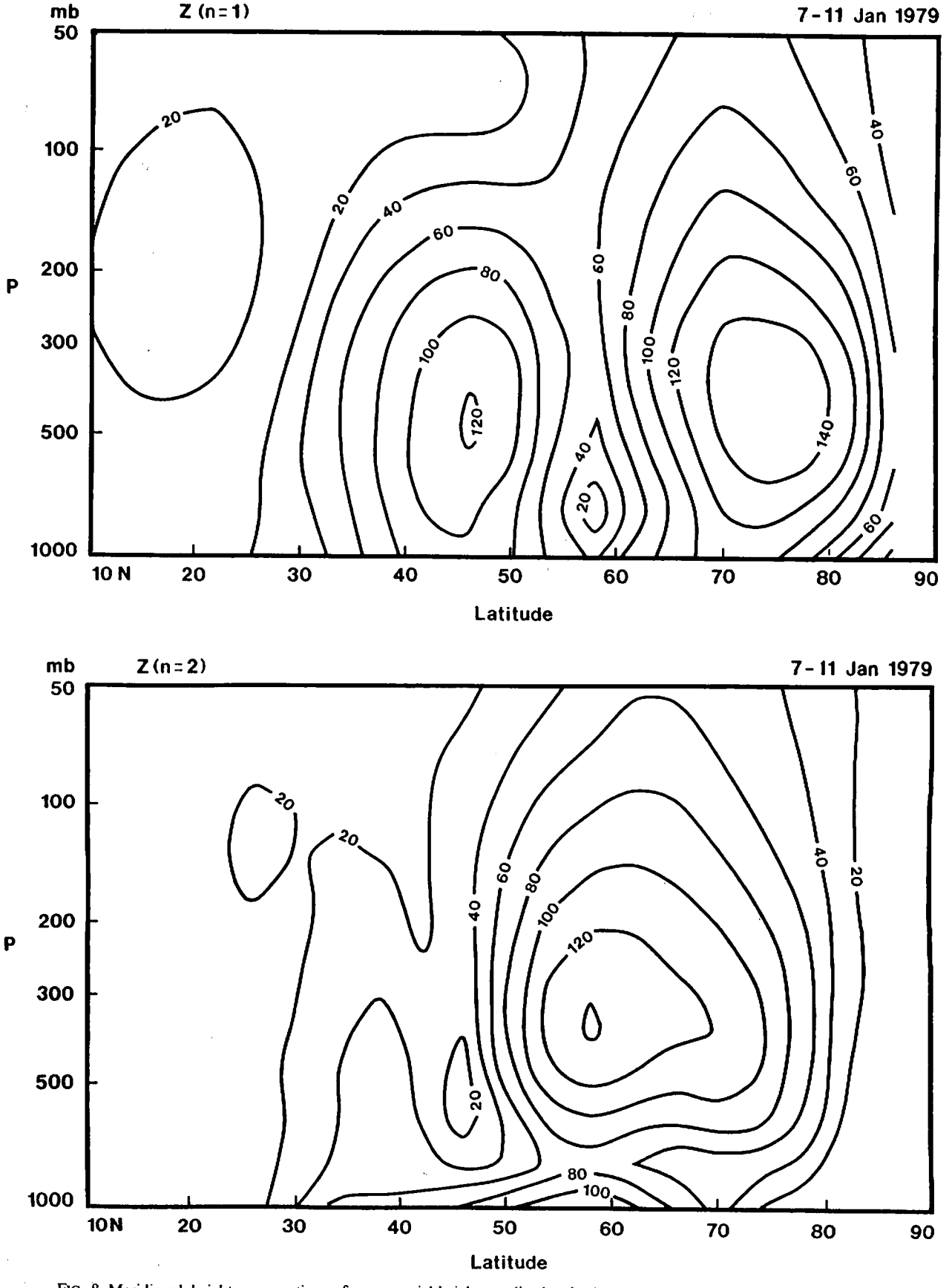


FIG. 8. Meridional–height cross sections of geopotential height amplitude $z$ in the Northern Hemisphere for $n = 1$ and 2. The values are observed 5-day means for 7–11 January 1979, multiplied by $(p/p_s)^{1/2}$, and expressed in the unit of $m$.

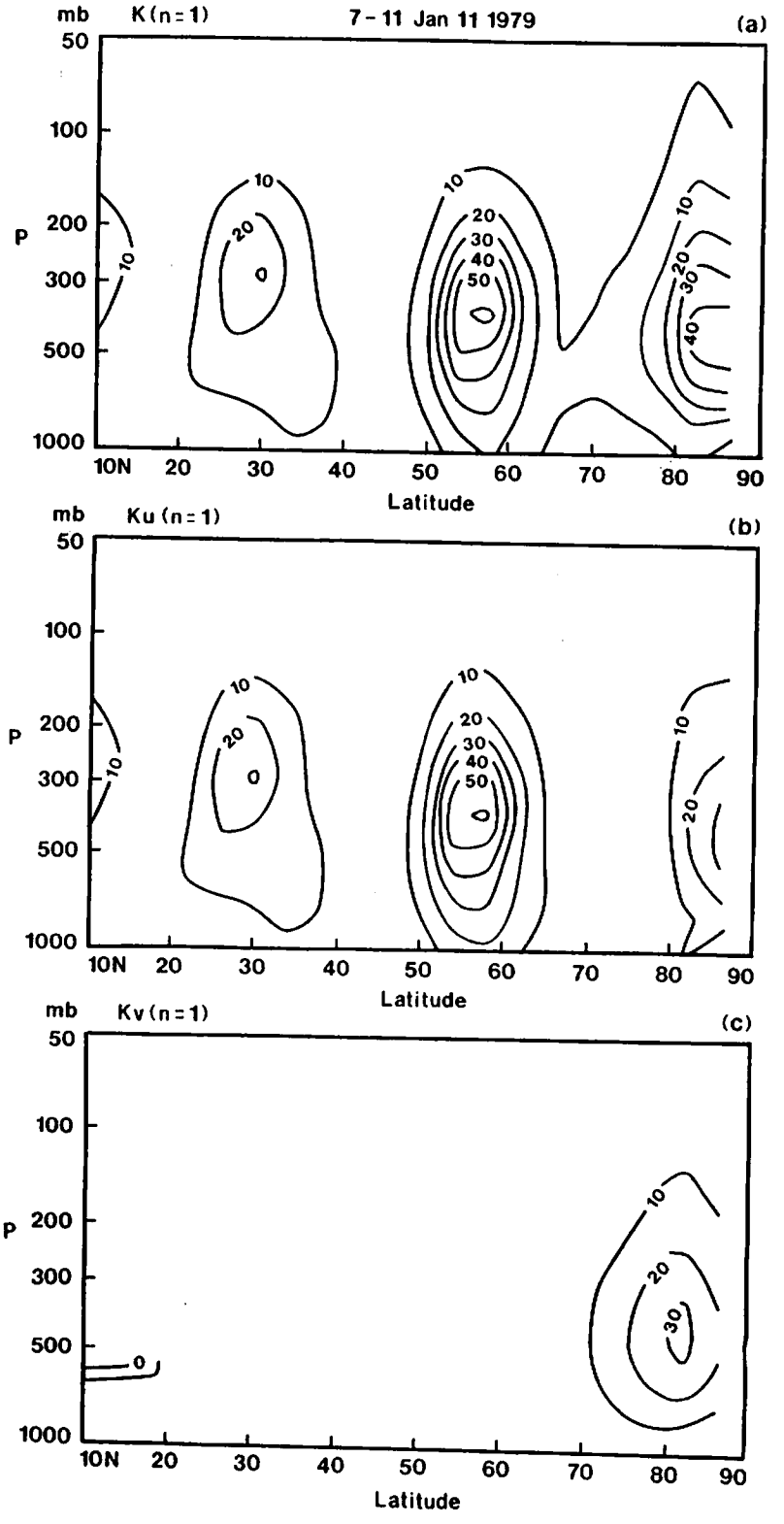


FIG. 9. Meridional-height cross sections of kinetic energy $K$, zonal component $K_u$ and meridional component $K_v$ in the Northern Hemisphere for $n = 1$. The values are 5-day means for 7–11 January 1979, multiplied by $\rho_0$ and expressed in the units of J m$^{-3}$.

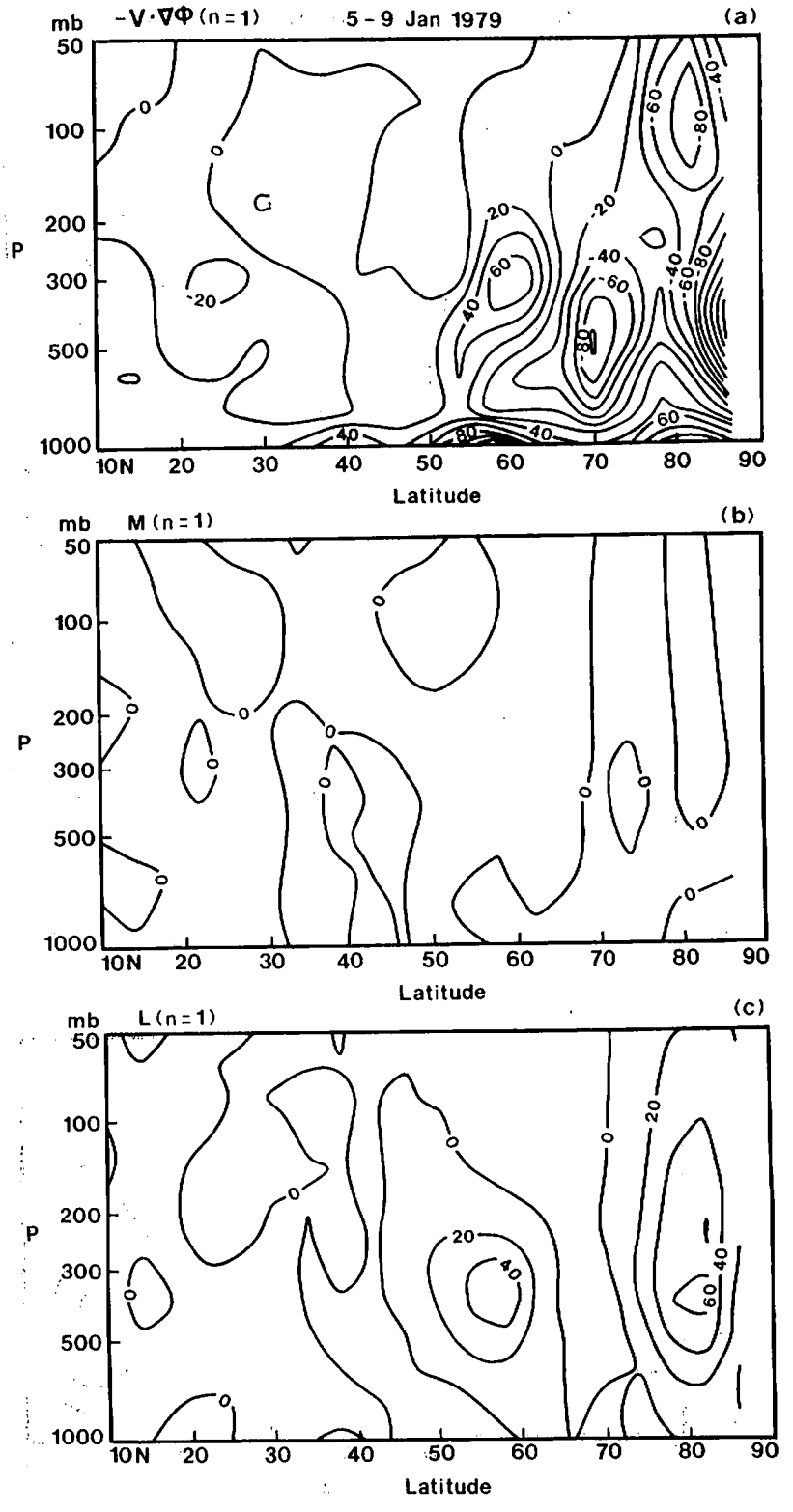


FIG. 10. As in Fig. 9, but for the kinetic energy production $-\mathbf{V}\cdot\nabla\phi$, wave–mean interaction $M$, and wave–wave interaction $L$ for $n = 1$. The values are observed 5-day means for 5–9 January 1979, multiplied by $\rho_0$, and expressed in the units of $10^{-5}$ W m$^{-3}$.

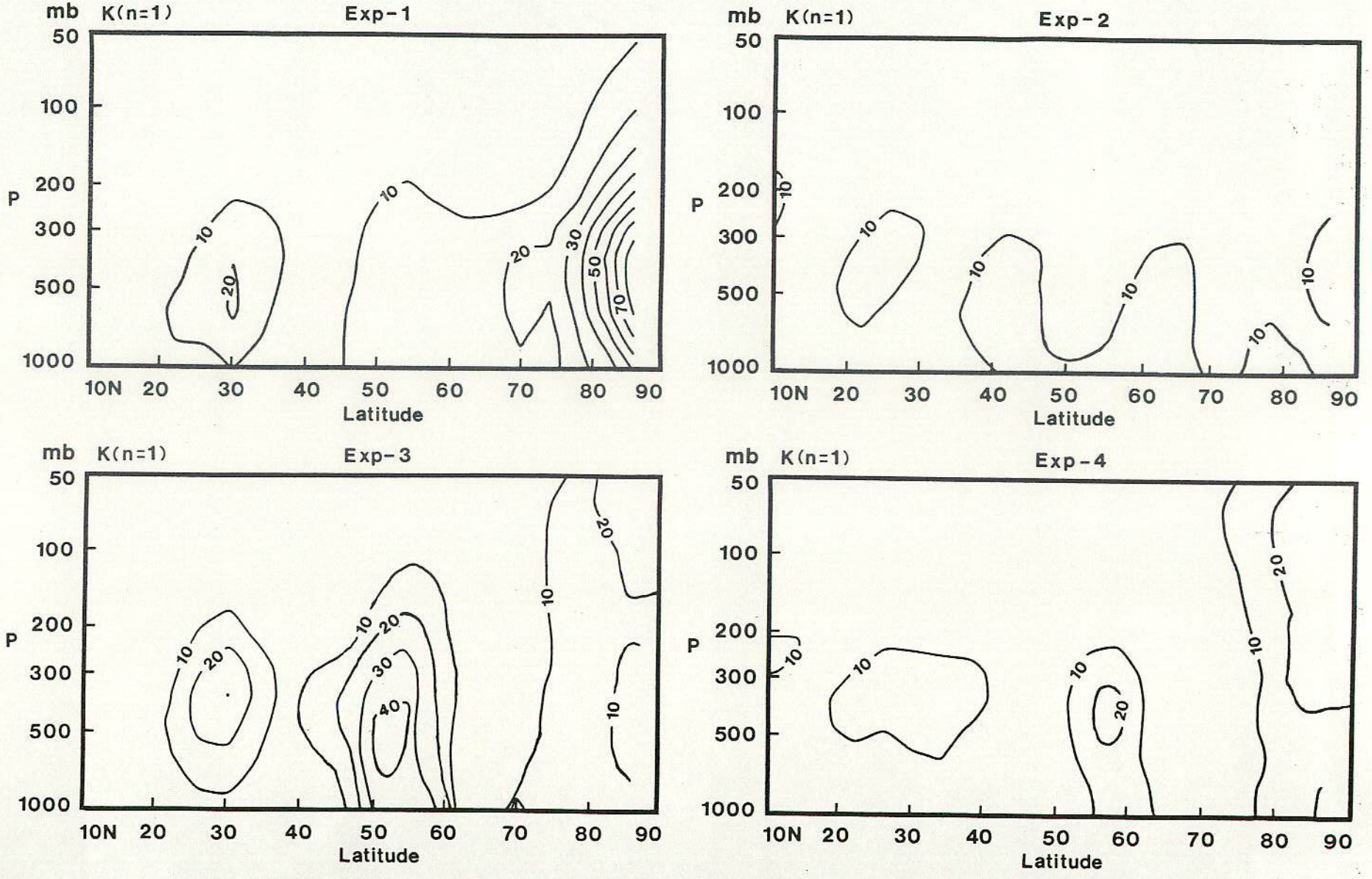


FIG. 11. Meridional–height cross sections of kinetic energy for four simulations during 7–11 January 1987 for $n = 1$ in units of J m$^{-3}$.

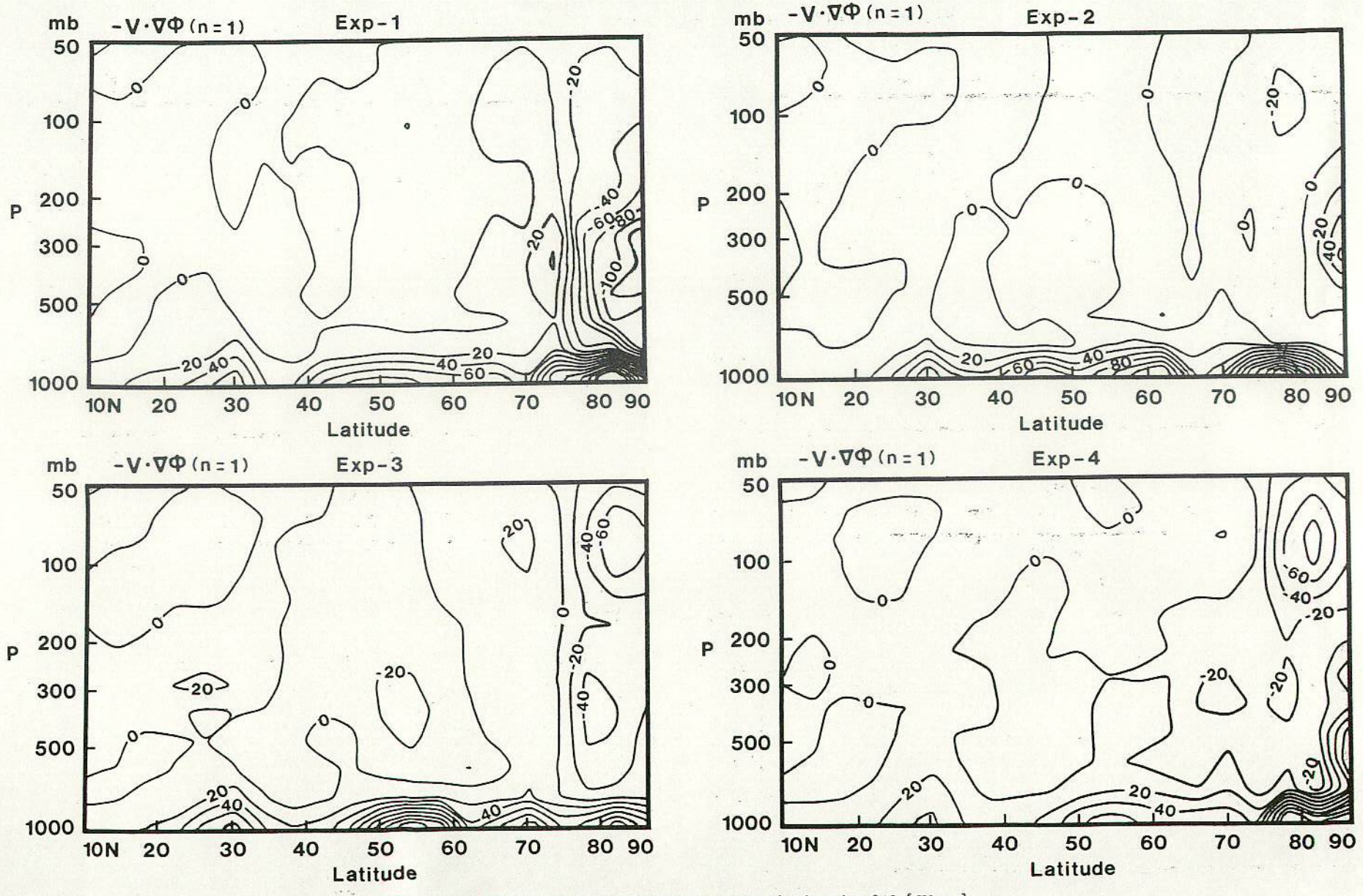


FIG. 12. As in Fig. 11, but for the kinetic energy production in units of $10^{-5}$ W m$^{-3}$.

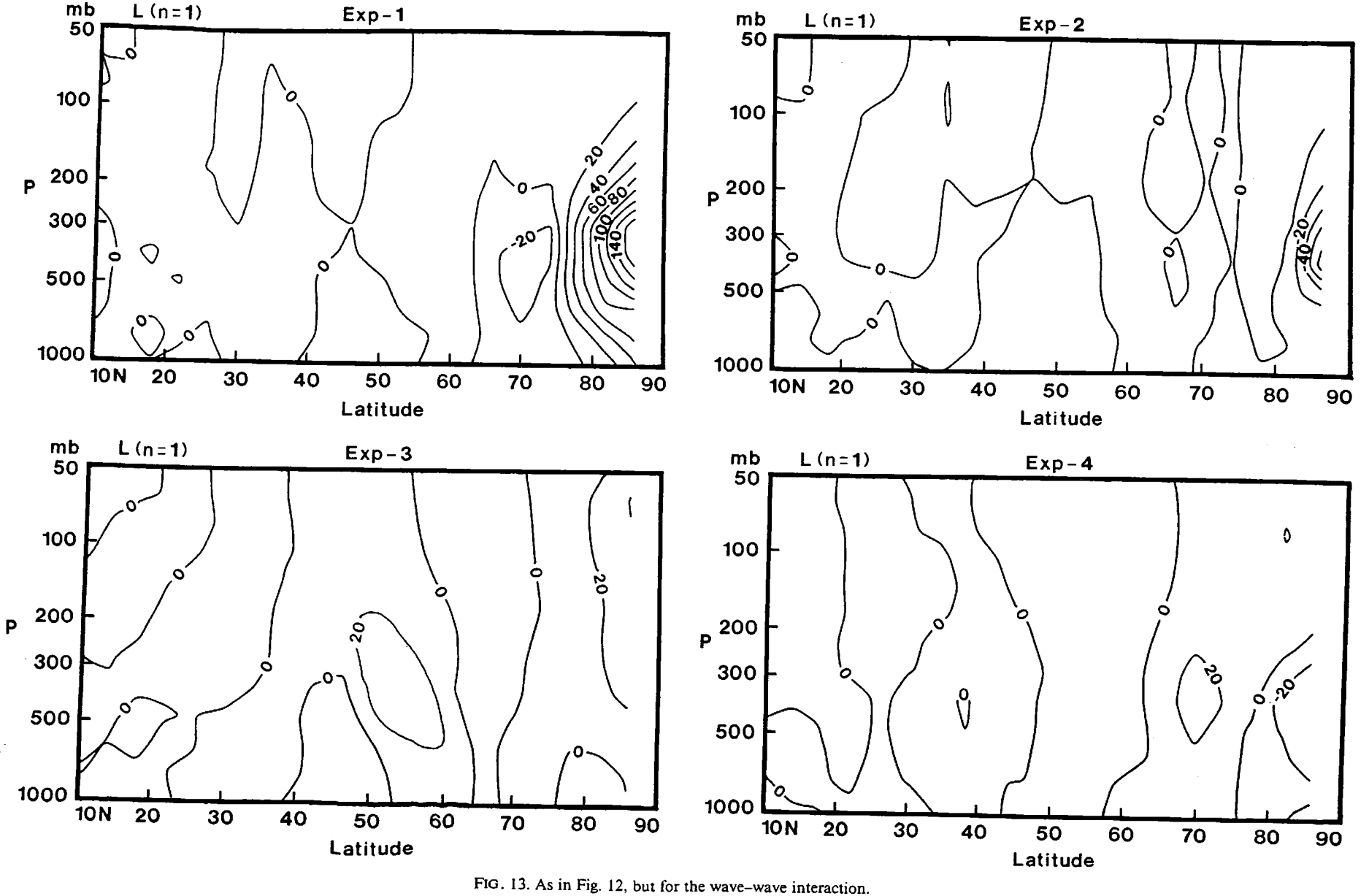


FIG. 13. As in Fig. 12, but for the wave–wave interaction.

4, which is also a simulation with the high resolution GCM, a weaker dipole of $K(1)$ than Expt. 3 is noted, but the pattern of existing dipole is clearer than Expts. 1 and 2 of the coarse grid GCM simulations. As is seen in Fig. 12, the distributions of $-\mathbf{V}\cdot\nabla\Phi$ for $n = 1$ in the simulations show the concentrated production of kinetic energy in the lower boundary of latitudes where $K(1)$ is large. However, $-\mathbf{V}\cdot\nabla\Phi$ in the upper troposphere is weak and the distribution is erroneous, reflecting the weak ageostrophic component of circulation in the simulation due to time integration by the Matsuno scheme (see Daley et al. 1985). The distributions of $L(1)$ of the simulations in Fig. 13 indicate $L(1)$ is generally much weaker than in the observation in Fig. 10. What are shown in cross sections of the simulations are consistent with the circulation patterns and spectral energy budgets (Table 3) in indicating that the high resolution of the model is needed to produce the proper wave–wave interaction to provide kinetic energy input at $n = 1$.

## 6. Barotropic–baroclinic conversions of energy

Temporal variations of barotropic ($m = 0$) and baroclinic ($m = 3$–$10$) energies in the zonal mean motion ($n = 0$), ultralong waves ($n = 1$–$2$) and synoptic waves ($n = 3$–$15$) over the Northern Hemisphere are illustrated in Fig. 14 after Tanaka and Kung (1988).

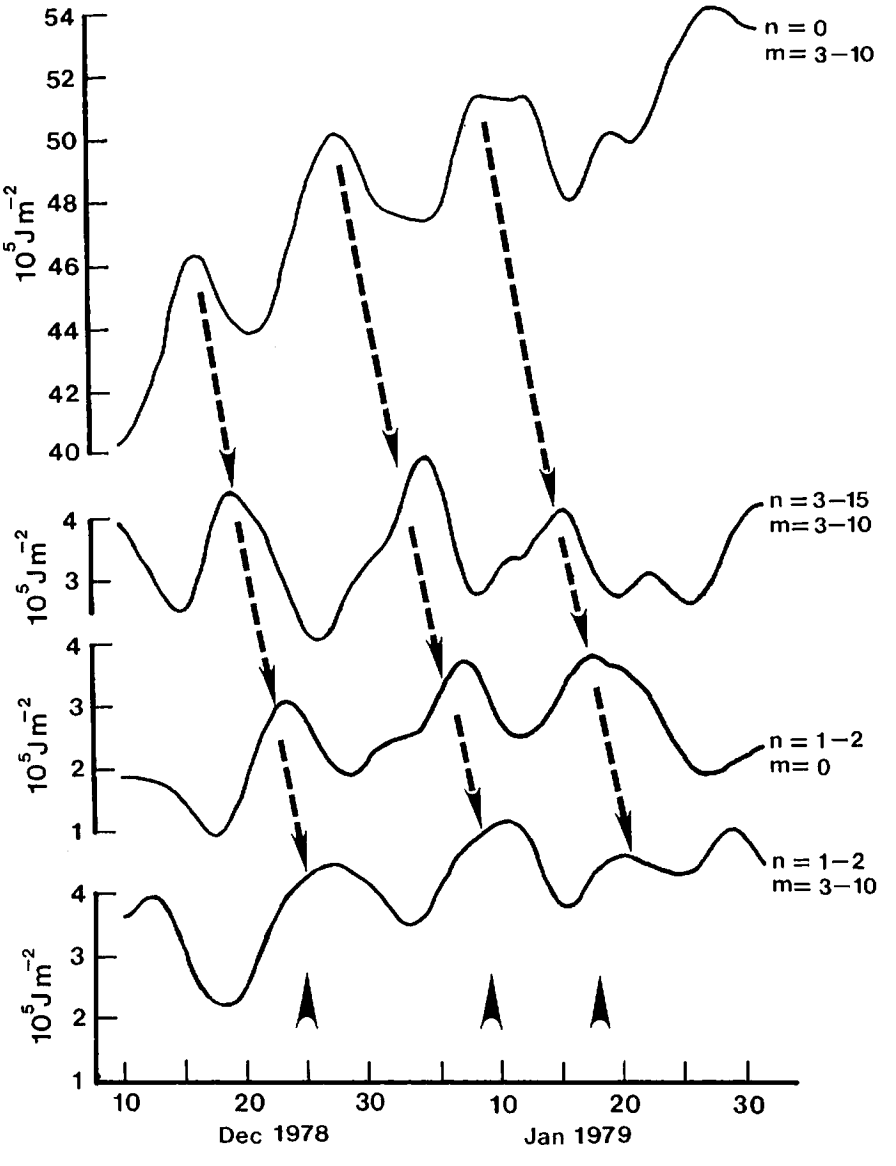


FIG. 14. Time series of barotropic ($m = 0$) and baroclinic ($m = 3$–$10$) energies for zonal mean motion ($n = 0$), ultralong waves ($n = 1$–$2$), and synoptic waves ($n = 3$–$15$) over the Northern Hemisphere from 10 December 1978 through 31 January 1979 after Tanaka and Kung (1988). Appearance for typical Rex blockings are marked by arrows over the time axis.

The time variation of the zonal baroclinic energy ($n = 0$, $m = 3$–$10$) indicates clear energy peaks at 16 and 28 December and 9 January superimposed on the seasonal trend. There are subsequent increases of baroclinic energy of synoptic waves in the time series ($n = 3$–$15$, $m = 3$–$10$) through a process of baroclinic instability. The time lag is about 5 days. The time variation of synoptic-scale barotropic energy ($n = 3$–$15$, $m = 0$) is not shown in the figure but it is almost in phase with the baroclinic energy. The barotropic energy of ultralong waves ($n = 1$–$2$, $m = 0$) increases three days later through the wave–wave interaction of kinetic energy, the process required for amplification of ultralong waves to form the blocking. The peaks of ($n = 1$–$2$, $m = 0$) are identified with the most intensified pattern of blockings as marked in the figure. After the full development of the blocking (i.e., after reaching the mature stage of the blocking), the baroclinic energy of ultralong waves peaks.

The orderly transfer of energy from the zonal baroclinic component to the barotropic component of ultralong waves in the normal mode expansion may be identified with processes observed in the standard zonal wavenumber domain. The zonal available potential energy is transferred into the synoptic-scale disturbances, converted to kinetic energy and then used to build up the barotropic energy of blocking in the ultralong waves during the blocking development. Based on time mean spectral energetics (Table 3), it is seen that synoptic-scale waves support the energy of planetary waves by means of wave–wave interaction. The time series in Fig. 14 further reveals evidence of the upscale energy cascade from synoptic-scale waves to planetary waves. The upscale energy cascade occurs when the energy supply is in a phase conducive to amplification of planetary waves. Also, as shown in Kung and Baker (1986), under the developed blocking situation the meridional heat transport increases dramatically, and this apparently leads to the peak of the baroclinic energy of ultralong waves in the mature blocking stage.

This orderly transfer of energy is not well simulated in the numerical experiments, as shown in Fig. 15. In simulations it is possible to follow the energy flow from the baroclinic component of the zonal motion to the baroclinic and barotropic components of the synoptic-scale waves. However, the buildup of the barotropic energy in the ultralong waves at the time of blocking development is difficult to follow in all simulations. This is consistent with the fact that in simulations, enough kinetic energy is available at the synoptic-scale range through baroclinic conversion, but the model tends to fail to provide adequate energy input at ultralong waves through the wave–wave interaction.

Despite the disturbed time series of energy components in simulations (Fig. 15), the parallel time series of the nonlinear interactions $A$ and $B$ in Fig. 16 indicate traceable transformations from the zonal baroclinic energy to the barotropic energy of ultralong waves. Around 5 and 25 January in Expt. 3, $\beta$ shows its maxima for ($n = 1$–$2$, $m = 0$), and as seen in Fig. 3 and Table 1, these are the periods when Expt. 3 generated the blockings. The first blocking is a reasonable simulation of the observed blocking, but the second blocking is dislocated in its longitudinal position. It may be noted, however, that Expt. 3 is the only simulation able to generate a second blocking after the first one. Expt. 2 also indicates a traceable energy transformation toward the barotropic energy of ultralong waves ($n = 1$ and 2). However, as seen from Table 3 the kinetic energy gain in mostly in $L(2)$ rather than $L(1)$.

As stated in Eq. (3) the effects of nonlinear interactions, $A$ and $B$, are balanced with the diabatic process $F$. For the barotropic component of ultralong waves, the largest portion of this process is expected to be the dissipation. Since $F$ is obtained as the residual term of Eq. (3), the dissipation is actually the energy sink or cascade from ($n = 1$–$2$, $m = 0$). The time series of energy components in Fig. 14 appear more disturbed than expected from time series of transformations in Fig. 15. It may indicate that, in addition to the weaker nonlinear wave–wave interaction at ultralong waves, the energy cascade process as implied by $F$ may be an additional problem in the numerical simulation of blocking, even with the high resolution model.

## 7. Concluding remarks

This study of Northern Hemisphere winter blocking episodes reveals considerable energetics differences between the simulations and the observation, and among simulations. In the simulations enough kinetic energy is available at the synoptic-scale range through the baroclinic conversion, but the models provide insufficient kinetic energy input from this source to $n = 1$ through the wave–wave interaction $L(1)$. The failure in simulating realistic blocking due to inadequate $L(1)$ can be attributed in part to inadequate grid resolution. The $4° \times 5°$ coarse resolution of the model results in a downscale energy cascade preventing a proper upscale input at $n = 1$.

Among the four simulations examined in this study, Expts. 3 and 4 by the high resolutions GCM data tended to generate realistically strong blockings with compatible energetics as in the observed blocking episode. It is also noted that Expt. 3 with the GLA initial data was able to amplify $n = 1$ to produce the second blocking during late January 1979 following the first one, although there was an obvious longitudinal dislocation of the second blocking.

The latitude–height cross sections of energy variables confirm that the dipole structure of the observed blocking is clearly described by $n = 1$, and further $L(1)$ maxima are located at the kinetic energy maxima of the dipole. However, in all simulations, such a dipole structure of energetics is either weak or nearly absent.

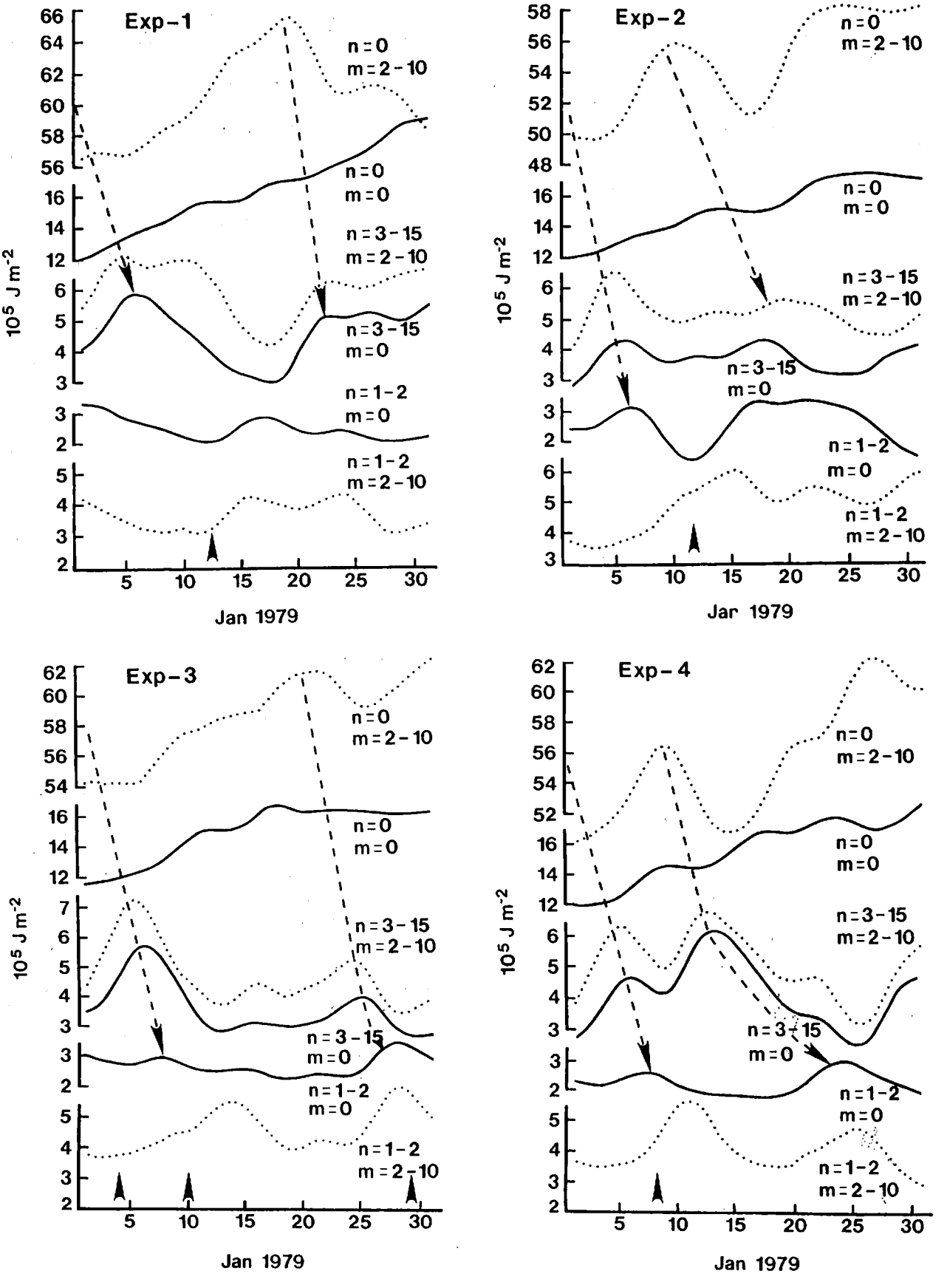


FIG. 15. As in Fig. 14, but for the four simulations. Baroclinic energy is the sum of baroclinic indices $m$ = 2–10.

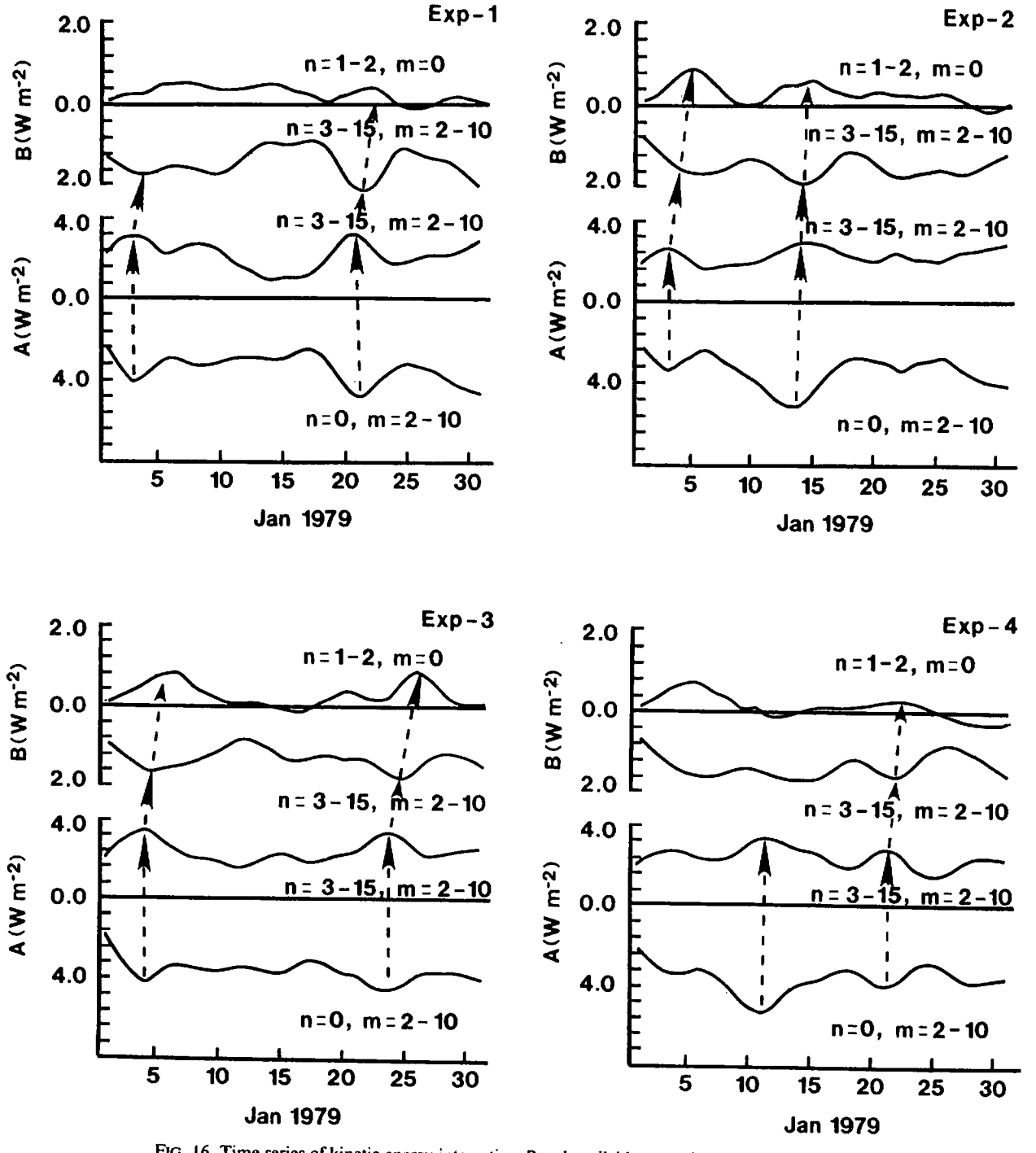


FIG. 16. Time series of kinetic energy interaction $B$ and available potential energy interaction $A$ for four simulations for the corresponding energy terms in Fig. 14.

Energetics of blocking development is further examined in a time series of barotropic and baroclinic components of energy and associated conversions. In the observed circulation an orderly transfer of energy is recognized from the zonal baroclinic component to the barotropic component of ultralong waves via synoptic-scale conversions. In the simulations, however, this orderly transfer of energy is not well simulated. The buildup of barotropic energy in ultralong waves at the time of blocking development is either too weak or unrecognizable. This is consistent with the trend of the model failing to provide an adequate energy input at ultralong waves through the wave–wave interaction.

*Acknowledgments.* The authors gratefully acknowledge the courtesy of Drs. K. Miyakoda and J. J. Ploshay of the Geophysical Fluid Dynamics Laboratory in providing the GFDL initial data, and the assistance of Y.

Brin and L. Takacs in the numerical experiments at the Goddard Space Flight Center. C. Da Camara of the University of Missouri—Columbia, provided valuable assistance in blocking identification. The authors are indebted to the anonymous reviewers, whose comments have led to a marked improvement of the paper. The authors are also thankful to S. Humphrey, G. Vickers, and D. Williams for their technical assistance. This research was performed at ECK Research Consulting Inc. under the National Aeronautics and Space Administration Contract NAS5-30128.

## REFERENCES

Baker, W. E, 1983: Objective analysis and assimilation of observational data from FGGE. *Mon. Wea. Rev.*, **111**, 328–342.

——, and Y. Brin, 1985: A comparison of observed and forecast energetics over North America. *Quart. J. Roy. Meteor. Soc.*, **111**, 641–663.

Bengtsson, L., 1981: Numerical prediction of atmospheric blocking—a case study. *Tellus*, **33**, 19–42.

Dalcher, A., and E. Kalnay, 1987: Error growth and predictability in operational ECMWF forecast. *Tellus*, **39A**, 474–491.

Daley, R., A. Hollingworth, J. Ploshay, K. Miyakoda, W. Baker, E. Kalnay, D. Dey, T. Krishnamurti and E. Barker, 1985: Objective analysis and assimilation techniques used for the production of FGGE IIIb analysis. *Bull. Amer. Meteor. Soc.*, 77, 532–540.

Hansen, A. R., and A. Sutera, 1984: A comparison of the spectral energy and enstrophy budgets of blocking versus nonblocking periods. *Tellus*, **36A**, 52–63.

Hollaway, G., and B. J. West, Eds., 1984: *Predictability of Fluid Motions*. American Institute of Physics, 612 pp.

Holopainen, E., and C. Fortelius, 1987: High-frequency transient eddies and blocking. *J. Atmos. Sci.*, **44**, 1632–1645.

Kalnay, E., R. Balgovind, W. Chao, D. Edelmann, J. Phaendtner, L. Takacs and K. Takano, 1983: Documentation of the GLAS fourth order general circulation model. NASA Tech. Memo 86064. [NTIS N8424028.]

Kalnay-Rivas, E., A. Bayliss and J. Storch, 1977: The fourth order GISS model of the global atmosphere. *Beitr. Phys. Atmos.*, **50**, 299–311.

Kung, E. C., 1988: Spectral energetics of the general circulation and time spectra of transient waves during the FGGE year. *J. Climate*, **1**, 5–19.

——, and W. E. Baker, 1986: Spectral energetics of the observed and simulated Northern Hemisphere general circulation during blocking periods. *J. Atmos. Sci.*, **43**, 2792–2812.

Lejenäs, H., and H. Økland, 1983: Characteristics of Northern Hemisphere blocking as determined from a long time series of observational data. *Tellus*, **35A**, 350–362.

Matsuno, T., 1970: Vertical propagation of stationary planetary waves in the Northern Hemisphere. *J. Atmos. Sci.*, **27**, 871–883.

Miyakoda, K., T. Gordon, R. Caverly, W. Stern and J. Sirutis, 1983: Simulation of blocking event in January 1977. *Mon. Wea. Rev.*, **111**, 846–869.

Saltzman, B., 1957: Equation governing the energetics of the larger scales of atmospheric turbulence in the domain of wavenumber. *J. Meteor.*, **14**, 513–523.

——, 1959: On the maintenance of the large-scale quasi-permanent disturbances in the atmosphere. *Tellus*, **11**, 425–431.

——, 1970: Large-scale atmospheric energetics in the wavenumber domain. *Rev. Geophys. Space Phys.*, **8**, 289–302.

Shapiro, R., 1970: Smoothing, filtering, and boundary effects. *Rev. Geophys. Space Phys.*, **8**, 359–387.

Shukla, J., 1981: Dynamical predictability of monthly means. *J. Atmos. Sci.*, **38**, 2547–2572.

Tanaka, H., 1985: Global energetics analysis by expansion into three-dimensional normal mode functions during the FGGE winter. *J. Meteor. Soc. Japan*, **63**, 180–200.

——, and E. C. Kung, 1988: Normal mode energetic of the general circulation during the FGGE year. *J. Atmos. Sci.*, **45**, 3723–3736.